Stirrer design for improving fluidization of cohesive powder

A time-resolved X-ray study

Wu, Kaiqiao; Kamphorst, Rens; Bakker, Anna; Ford, Jasper; Wagner, Evert C.; Ochkin-Koenig, Olga; Franck, Miika; Weis, Dominik; Meesters, Gabrie M.H.; van Ommen, J. Ruud

DOI
10.1016/j.ces.2024.120069

Publication date
2024

Document Version
Final published version

Published in
Chemical Engineering Science

Citation (APA)
Wu, K., Kamphorst, R., Bakker, A., Ford, J., Wagner, E. C., Ochkin-Koenig, O., Franck, M., Weis, D., Meesters, G. M. H., & van Ommen, J. R. (2024). Stirrer design for improving fluidization of cohesive powder: A time-resolved X-ray study. *Chemical Engineering Science*, *294*, Article 120069. https://doi.org/10.1016/j.ces.2024.120069

Chemical Engineering Science 294 (2024) 120069

Contents lists available at ScienceDirect

Chemical Engineering Science

journal homepage: www.elsevier.com/locate/ces

Stirrer design for improving fluidization of cohesive powder: A time-resolved X-ray study

Kaiqiao Wu [a,b,c,*], Rens Kamphorst [b], Anna Bakker [b], Jasper Ford [b], Evert C. Wagner [b], Olga Ochkin-Koenig [d], Miika Franck [d], Dominik Weis [d], Gabrie M.H. Meesters [b], J. Ruud van Ommen [b,**]

[a] Department of Chemical Engineering, Guangdong University of Technology, Guangzhou, 510006, China
[b] Department of Chemical Engineering, Delft University of Technology, Delft, 2629HZ, the Netherlands
[c] Guangdong Provincial Laboratory of Chemistry and Fine Chemical Engineering Jieyang Center, Jieyang, 515200, China
[d] BASF SE, Ludwigshafen am Rhein, 67063, Germany

ARTICLE INFO

Keywords:
Stirred fluidization
Cohesive powder
X-ray imaging
Vibration
Gas channel

ABSTRACT

Stirring has been recognized in the literature as a promising technique for facilitating fluidization of cohesive powders, via inputting additional energy to counteract interparticle forces. However, the influence of operating conditions and stirrer configurations on flow behavior remains largely unknown, which impedes the practical implementation of stirred fluidization. Utilizing X-ray imaging, this research demonstrates that stirring enhances fluidization in cohesive micron-silica powder (Sauter mean diameter $D_{32} = 7.9\,\mu m$) by collapsing the powder packing structure, and transitioning channeling beds into bubbling states. Comb-like configurations featuring fewer stirrers and blades, placed in the bottom region, have shown to be highly effective. Excessive stirring can lead to air pockets and a compacted phase of particles on the column walls, undermining the interaction between particles and stirrers. Additionally, the experiments show that maximizing the sweeping coverage, employing complex asymmetrical configurations, and avoiding tortuous gas pathways are preferable.

1. Introduction

Fluidization is a popular technique to process solids for various applications in industry, where exceptional interphase mixing and heat and mass transfer are paramount. Smooth fluidization is easily attainable with sand-like particles, whereas it becomes rather troublesome to effectively aerate fine particles because of their intrinsic cohesiveness. Strong interparticle forces, such as capillary and van der Waals forces, dominate the collective behavior of fine particles, resulting in the formation of agglomerates (Raganati et al., 2018; Kamphorst et al., 2023). When fluidizing fine powders, individual particles or agglomerates tend to adhere together, forming internal cracks and channels, which results in a substantial portion of the fluidizing gas to bypass, undermining the gas-solids interaction (van Ommen et al., 2012).

Incorporating additional degrees of freedom allows for enhanced flexibility in manipulating fluidization. A range of "assistance methods", imposing various forces and forms of energy on the system, has been demonstrated to be effective in improving fluidization of fine powders (van Ommen et al., 2012; Zhang, 2009; van Ommen et al., 2009). These approaches can be classified based on the mode of manipulation, which involves imposing dynamic or geometrical constraints on the gas or solid phase, and modifications to forces, such as contact force (e.g., particle-particle and particle-wall), surface force (e.g., particle-fluid), or body force (e.g., external force fields and gravitational pull) (Francía et al., 2021). External actuators have been explored, with numerous successful attempts documented in the literature, including vibration (Zhao et al., 2020; Cruz et al., 2005; Kamphorst et al., 2024b), pulsation (Wu et al., 2017; Khosravi Bizhaem and Basirat Tabrizi, 2013), stirrer mixing (Zhao et al., 2020; Kariman et al., 2013), high-speed jet flow (Hong et al., 2005; van Ommen et al., 2013; Quevedo et al., 2010), and doping of flow conditioner (Alavi and Caussat, 2005; Zhou and Zhu, 2019; Yin et al., 2008). Nonetheless, devising a universal method for fluidizing cohesive powders remains a challenge, as the type of cohesion, scalability,

* Corresponding author at: Department of Chemical Engineering, Delft University of Technology, Delft, 2629HZ, the Netherlands.
** Corresponding author.
E-mail addresses: K.Wu-3@tudelft.nl (K. Wu), J.R.vanOmmen@tudelft.nl (J.R. van Ommen).

https://doi.org/10.1016/j.ces.2024.120069
Received 25 December 2023; Received in revised form 25 March 2024; Accepted 26 March 2024
Available online 2 April 2024

energy consumption, and instrumentation requirements varies between different applications.

In comparison to other assistance techniques, stirring offers advantages in terms of scale-up practices, operation and effective length, and practicality of integration with existing reactor units. Stirrers function as moving internals to agitate particulate flows, transmitting mechanical energy through particle-boundary interaction. Nevertheless, their performance largely relies on the operating conditions and stirrer configurations. For instance, there is no universally applicable rotation speed. Previous research reports that, in columns with diameters ranging between 3 cm and 7 cm, increasing stirring speed mitigates agglomeration and channeling, resulting in a reduced terminal velocity and minimum fluidization velocity for Geldart C micro-powders (Kim and Han, 2006), while improving bed dilation (Kariman et al., 2013) and promoting a vigorous bubbling fluidization state for nano-powders (Zhao et al., 2020). However, in columns of similar sizes, excessively high rotation speeds (e.g., faster than 100 rpm) have been found to significantly increase the particle entrainment rate in fluidizing Geldart C type micro-powders (Yang et al., 2013). Additionally, a tendency to compress particles against the column walls was observed, resulting in the formation of the compact layers of solids, indicated by an overshoot in the bed pressure drop signal (Alavi and Caussat, 2005). On the other hand, a low rotation speed (e.g., 30 rpm), irrespective of stirrer geometries, has been observed to yield insufficient impact on agglomerates to overcome interparticle forces of micro-powders larger than 1 μm (Alavi and Caussat, 2005), although such a speed has been shown fast enough to promote fluidization of sub-micron and nano-powders smaller than 1 μm (King et al., 2008). The placement of the stirrer also plays a crucial role. An impeller-type stirrer was investigated and considered most effective when positioned in the bottom region of the bed, e.g., within approximately 1 cm from the base of a 45 cm deep column (Godard and Richardson, 1969). It is hypothesized that the stirrers sweep particles into the initial channels, which subsequently break down. However, in half a column (semi-circle or a 'D' shape when viewed from above) with a diameter of 20 cm, improved fluidization quality and reduced minimum fluidization velocity of micron cohesive particles (16 μm LiF powder used in the study) were also found with the impeller placed at a higher position (e.g., at 70% static bed height) (Hu et al., 2020). This study also concluded that gas channels develop and become too persistent to break when the stirrer is mounted too high (e.g., at 86% static bed height), as indicated by a significant reduction in the measured pressure drop. Studies on stirred fluidization of fine, cohesive powders are scarce, and primarily rely on pressure drop measurements and visualization on the surface layers through transparent walls. Nevertheless, the local gas channeling and powder structures complicate the interpretation of pressure signals, making it challenging to associate with the impact induced by stirring on the hydrodynamics. Furthermore, surface layers, which experience significant boundary effects, do not accurately represent the bulk flow behavior, and fine particle clouds have a tendency to adhere to walls, rapidly causing blurred or obstructed visibility.

Non-intrusive imaging and tomography techniques, extensively applied in medical and technical practices, such as electrical capacitance tomography (Makkawi and Wright, 2002; Chandrasekera et al., 2012), magnetic resonance imaging (Boyce et al., 2016; Penn et al., 2019), and X-ray imaging and computational tomography (XRT) (Mudde, 2010), offer opportunities to overcome the constraints of observational limitation and access into system hydrodynamics (van Ommen and Mudde). These technologies allow for a direct visual exploration into the bed characteristics in 3-D opaque systems, not only monitoring the detailed time evolution of apparent phenomena, such as flow pattern and bubble motion, but also quantitatively measuring particle-level features, including solid fraction distribution and particle segregation. Consequently, they facilitate understanding of systems with complex hydrodynamic behaviors and fundamental mechanisms. In terms of studying gas-solid system, among the mentioned techniques, X-ray imaging excels by offering a higher spatial resolution and identification of material contrast (van Ommen and Mudde). This technique has been widely applied since the 90 s to study the gas-solid fluidization of various powders (Ma et al., 2019; Mema et al., 2020) and structural geometries (Maurer et al., 2015; Helmi et al., 2017). With the X-ray beams attenuating according to the local solid fraction, it is possible to attain a temporally resolved solid distribution of fluidization, which allows for the direct inspection and tracking of local hydrodynamic events within a cylindrical apparatus, like the one employed in this study (Saayman et al., 2013).

In this study, a comprehensive experimental investigation into the effects of stirring on the fluidization of cohesive powders by varying design parameters and operating conditions was conducted. The fluidization behavior is thoroughly compared across various design variables, including the number of stirrers, number of blades, rotation speed and geometry. Two-dimensional (2D) fast X-ray imaging was performed in conjunction with pressure drop and bed expansion measurements to capture the temporal evolution of flow patterns and identify in-situ hydrodynamic events, such as solid distribution, gas bubble development, and channel formation. The results serve as a valuable guide for designing optimal stirrers for applications of solid processing and provide opportunities for validating models of simulating fluidization of cohesive powders.

2. Experimentation and methodology

2.1. Experimental setup

Fig. 1 depicts a schematic representation of the experimental arrangement. Experiments were conducted using a Plexiglas column with an inner diameter D of 5 cm. Two 3 mm thick porous plates (SIKA-R 3 AX, Sintertech) were used to couple the column to a plenum chamber situated below and a breakout box positioned above. The porous plates were cleaned using an ultrasound bath before use. Furthermore, particles entrained within the fluidized bed were captured by the porous plate positioned at the top of the column. To ensure safety, a wash bottle and a HEPA powder filter were installed downstream prior to discharging the fluidizing gas into the atmosphere.

The column was mounted onto a vibration table, which was utilized for initialization of fluidization in certain experiments. The particles were fluidized at room temperature with dry nitrogen gas, which was regulated using a mass flow controller (Bronkhorst F-202AV). An in-house LabVIEW program managed the data acquisition system, which connected to both the flow controller and pressure transducers (OMEGA-PX419). A motor was placed on top of the breakout box, with the lowest tip of the shaft mounted 5 mm above the distributor. The shaft used in this study was made of metal, effectively functioning as a grounding rod and mitigating the triboelectric charging of particles induced by stirring. It is therefore expected that the contribution of electrostatic forces to the observed fluidizaiton behavior to be minimal.

2.2. X-ray image processing

Fast X-ray imaging serves as a non-invasive and hard field technique to effectively monitor system hydrodynamics. The column was positioned in between an X-ray generation tube and a scintillation detector panel, as shown in Fig. 2. The distance between the source tube and center of the column was set at 100 cm. The X-ray source used was YXLON Y.TU 160-D06 tube with a maximum voltage of 150 kV and a maximum anode current of 12 mA. In this study, a voltage of 120 kV and a current of 1.9 mA were selected to ensure the X-ray intensity remained sufficiently high after passing though the full bed, yet did not surpass the maximum limit of the detector when passing through an empty column. The X-ray detector plate utilized is a Theledyne Dalsa Xineos-3131 model, featuring a sensitive area measuring 307 mm× 302 mm and a resolution of 1548 × 1524 pixels. Each pixel has dimensions of 198 μm ×

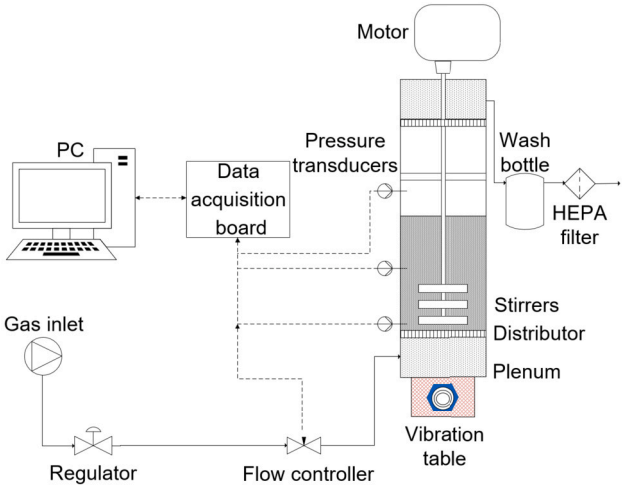

Fig. 1. Schematic representation of the experimental setup.

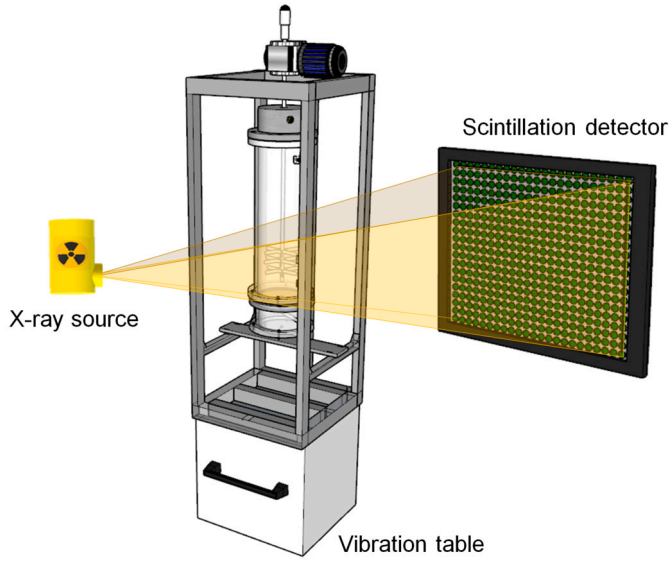

Fig. 2. Schematic representation of the X-ray imaging setup. The column is placed in between the X-ray source and detector.

198 μm. In this work, a field of view of 1548 × 500 pixels is used. The raw images were acquired at a frame rate of 65 Hz, which is considered sufficient for monitoring the system hydrodynamics, as the majority of hydrodynamic events occur below 10 Hz (Wu et al., 2023a).

X-ray beams pass through gas-solid suspensions, their attenuation being directly proportional to the mass of the material present within the pathway (Mudde, 2010). For each experiment, the attenuated X-ray beams were measured at the detector panel to construct a 2D intensity map of the field of view. The attenuation of X-ray beams follows the Lambert-Beer law:

$$I = I_0 \exp(-\mu d) \tag{1}$$

where I_0 and I are the intensity of X-ray beams before and after penetrating loaded material of a thickness d, μ is the attenuation coefficient associated with the material properties. Theoretically, deviation from the correlation is expected, as X-rays are poly-chromatic. However, a calibration test shows that this deviation is minimal (see section 1 of the Supplementary Material for the calibration procedure).

The X-ray attenuation provides a map of the gas fraction. Considering the same solid material, the local normalized gas fraction, denoted as ε, is expressed as a line integral extending from the X-ray source to the specific pixel on the detector:

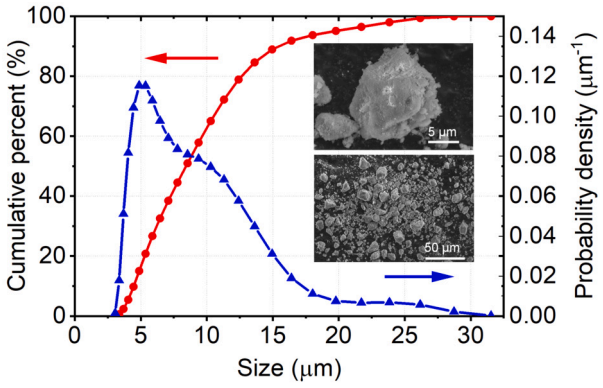

Fig. 3. Volume-based particle size distribution and cumulative distribution of the silica powder. Sauter mean diameter D_{32} is 7.9 μm. The inserted photos are the SEM images of the silica powder.

$$\varepsilon = \frac{d_f - d_m}{d_f} \tag{2}$$

where d_f and d_m represent the solid length (i.e., the distance of the X-ray beam traveling through solids) of the full bed and measurement, respectively. As per Eq. (1), these solid lengths can be obtained by measuring two reference intensity profiles:

$$d_f = \mu^{-1} \ln\left(\frac{I_{empty}}{I_{full}}\right)$$
$$d_m = \mu^{-1} \ln\left(\frac{I_{empty}}{I_{meas}}\right) \tag{3}$$

where I_{empty} is for an empty column, and I_{full} is for a fully loaded column. I_{meas} is for the measurement column. By employing a two-point calibration protocol with these two reference profiles of X-ray intensity, the gas fraction ε can be computed using the following expressions:

$$\varepsilon(I_{meas}) = \frac{\ln(I_{meas} / I_{\text{full}})}{\ln(I_{\text{empty}} / I_{\text{full}})} \tag{4}$$

Note that the range of ε, as per the definition, lies between 0 and 1, standing for the close packing of the powder and pure gas, respectively. In order to obtain a reproducible full reference, the loaded powders were vibrated for 10 min to approach a close packing state without the presence of stirrers. In the subsequent gas fraction maps, low attenuation of X-rays is represented by deep blue colors, signifying low solid concentrations. On the other hand, high attenuation of X-rays is represented by red colors, denoting high solid concentrations. The projected area of both the stirrers and shaft consistently appearing in deep red, due to higher attenuation, have been excluded from the analysis.

Given a symmetrical configuration, the projections obtained from various angles are expected to be identical. Validation experiments were conducted by shooting X-ray simultaneously from three detector-source pairs, with each pair being evenly spaced by 120 degrees. The outcomes confirmed that the flow patterns are indeed symmetrical, and that a projection from a single angle is sufficiently representative (see section 2 of the Supplementary Material for the validation experiments).

2.3. Powder properties

Commercially available Geldart C Silica powder (CWK Bad Köstritz) was employed in this study. Laser diffraction particle analyzer measurements reveal a mono-peak size distribution, characterized by a Sauter mean diameter of 7.9 μm, as depicted in Fig. 3. The cohesive silica powder tends to form agglomerates upon close contact. The scanning electron microscopy (SEM) images of the fresh powder confirm

the presence of intricately shaped primary agglomerates (see figures inserted in Fig. 3). The silica powder is porous, with a skeletal density of 1900 kg/m^3. The theoretical minimum fluidization velocity U_{mf} is determined to be 0.002 cm/s as per the Gidaspow correlation (Gidaspow et al., 1991). However, preliminary tests show channeling in the powder bed up to 7 cm/s, making it impractical to determine the experimental U_{mf}. The bulk density is 134 kg/m^3, determined by filling a measuring column without consolidation. The dynamic angle of repose is measured to be 50°, using a rotating drum at 30 revolutions per minute. This angle indicates poor flowability according to the Carr classification (Beakawi Al-Hashemi and Baghabra Al-Amoudi, 2018).

2.4. Fluidization properties

To facilitate the evaluation of fluidization, the pressure drop across both the entire and lower section (8.5 cm above the distributor plate) of the fluidized powder bed was continuously monitored using two pressure transducers. Pressure oscillations were recorded at a sampling rate of 1000 Hz. Oscillations in the pressure time series are induced by the periodic rotation of stirrers and the bubbling events. Signal analysis is conducted in both time and frequency domains, as illustrated by time-averaged and power-spectrum plots (van Ommen et al., 2011; Wu et al., 2023a). Furthermore, for fluidization, dominant hydrodynamic events typically occur at frequencies below 10 Hz (van Ommen et al., 2011).

For a 2D projection of the flow pattern, a bubble is defined as the area consisting of pixels where the gas fraction exceeds a threshold determined from the surroundings. An in-house MATLAB code is used to identify the bubbles by adaptive thresholding (Bradley and Roth, 2007). The bubbling probability density is constructed:

$$p_b(x,y) = \frac{1}{N_{\Delta t}\Delta x \Delta y} \sum_{t=t_0}^{t_0+\Delta t} F_b(x,y,t) \tag{5}$$

where F_b is the bubble flag, which is equal to one for a bubble pixel and zero for an emulsion pixel. $N_{\Delta t}$ is the number of X-ray imaging frames between t_0 and $t_0 + \Delta t$.

In addition, with the gas fraction ε obtained from the X-ray imaging, a time-averaged gas fraction profile $\overline{\varepsilon}$ can be computed as follows:

$$\overline{\varepsilon}(x,y) = \frac{1}{N_{\Delta t}} \sum_{t=t_0}^{t_0+\Delta t} \varepsilon(x,y,t) \tag{6}$$

2.5. Stirrer configurations

Various stirring parameters were investigated independently using a (comb-form configuration) modular design that allows decoupling design parameters and producing measurable effects. The modular design employs basic axial blade stirrers as building blocks, inspired by the work conducted by Kuipers et al. (1996), in which the authors investigated the impact of various axial stirrers on the fluidization of heavy potato starch (mean volume-based diameter around 50 μm). The dimensions of the stirrer were adapted to suit the column in this study, and set to a diameter of 41 mm, which considers a certain shaft wobble and results in a gap of 4.5 mm between the blade tip and the column wall for each side. All stirrers were 3D-printed with Polylactic Acid-Polymer (PLA) material. An additional ring disc was affixed to the shaft to minimize the wobbling effect, located at 30 cm above the distributor plate, which is beyond the maximum bed height reached by the bed. Multiple stirrers could be flexibly mounted and stacked with a separation of 6 mm between the neighboring stirrers, secured by two nuts. Example stirrers are depicted in Fig. 4.

2.6. Experimental design

To prepare for the experiments, the unfluidized powder was initially sieved through a 600 μm mesh to collapse any large, existing agglomerates and ensure an equal state of initial aeration. For each experiment, a new batch of sieved powder of 21 g was loaded, constituting a static bed height H_0 of approximately 10 cm ($H_0/D = 2$). The performance of the stirrer design is evaluated from two different perspectives: the ability to initialize and sustain fluidization. The initialization phase concerns the stirrer configuration's effectiveness in disrupting pre-existing bed structures, such as cracks and channels induced by the shaft placement and powder loading protocols, and initiating the aeration of particles. Conversely, the maintenance phase focuses on the stirrer's capacity to sustain a consistent state of complete fluidization. The detailed operating protocols are listed in Fig. 5.

To comprehensively identify the influence of various stirrer configurations on fluidizing cohesive powder, a series of experiments was conducted under different conditions, including rotation speeds, number of blades, and stirrer arrangements. Other design variables, such as attachment angle of blades and length of blade, while important, are less contentious in designing and fall outside the scope of this study to determine the optimal stirrer dimensions or test every possible configurations. The observed fluidization was compared to evaluate the significance of each parameter on flow behavior. The experiment conditions tested are listed in Table 1. The fluidization observed in the highlighted experiment (conditions marked in bold in Table 1) serves as a reference for comparing the effects of various stirring conditions. Each experiment was conducted at least in duplicate to ensure reliability and reproducibility of the results.

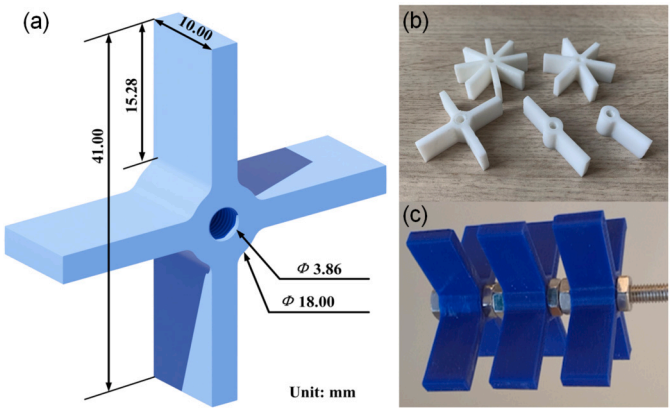

Fig. 4. 3D-printed modular stirrers: (a) dimensions of the four-bladed modular design, (b) modular stirrers with different number of blades, and (c) an example of stacked stirrers.

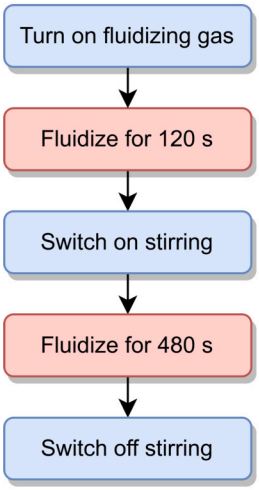

Fig. 5. Operating procedures for the stirring fluidization experiments. U = 3.1 cm/s.

Table 1
Experimental conditions investigated.

Stirring parameter*	Value
Rotation speed [rpm], N	35; 70; **130**; 160; 230
Number of blade [-], B	1; 2; **4**; 6; 8
Number of stirrer [-], S	1; 2; **3**; 6

* The conditions of the reference case are present in bold.

3. Results and discussion

A comparative study of the stirrers' capability to initialize and sustain effective fluidization is conducted concerning the key fluidization properties, such as flow pattern, solid distribution, bed expansion, and pressure drop. Based on the analysis, a set of criteria for stirrer design is proposed and then examined based on the improved stirrer configurations.

3.1. Hydrodynamics of the unassisted and vibro-fluidized beds

For comparison purpose, unassisted and vibro-fluidization experiments were carried out, with no stirrer present in the system. The fluidizing gas was introduced at the beginning in both experiments. For vibro-fluidization, the vibration was activated at 120 s. Notable differences in the flow patterns arise between the unassisted and vibro-fluidization of cohesive powder. When subjected to dry nitrogen gas without vibration, micron-silica particles initially form a plug and the entire powder bed rises in the column. Subsequently, upon hitting the top plate, this plug collapses, causing the elevated powders to fall and settle on the distributor plate, resulting in a slightly dilated bed with disorganized internal cracks.

Fig. 6 shows the time-evolving flow patterns over a 540 s fluidization with a superficial gas velocity $U = 3.1$ cm/s after the plug has collapsed, and the powder has settled. In absence of external assistance, the powders remain predominantly stationary, despite the presence of a fluidizing gas. Mechanical vibration is shown able to initiate fluidization, resulting in significant bed expansion and bubbling. Nevertheless, stratification of the powder occurs rapidly, with two distinct flow regions appearing over time, as depicted in Fig. 6b. Due to vibration, the bottom layer of powders progressively compacts against the distributor plate, causing a significant reduction in the gas fraction ε at normalized Y-position, $Y/D = 1.0$. In addition, the dilute phase in the top bed also decreases in depth and gas fraction, eventually leading to incomplete fluidization, showing poor sustainability. Similar fluidization behavior has been observed in a larger vibrated column (Wu et al., 2023b).

3.2. Effect of rotation speed

To investigate the impact of rotation speed on fluidization, experiments were conducted employing a configuration consisting of three stirrers, each with four radial blades (as displayed in Fig. 4c), operating at speeds of 35 rpm, 70 rpm, 130 rpm, 160 rpm and 230 rpm. The results reveal that varying rotation speed has distinct effects on the initialization of fluidization, as shown in Fig. 7.

For the beds initiated by stirring, it was observed that as the stirrer begins to rotate, the rotating blades disrupt and break up the primary packed structure within the sweeping region into fragments or agglomerates. These fragments subsequently become fluidized, traveling towards the upper region of the bed. Simultaneously, the structure of packed particles located above the sweeping region descends and collapses layer by layer upon contact with the blades. A good representation of this phenomenon can be seen in Fig. 7a for 160 rpm at 120 s, where the bottom section of the bed is agitated by the sitter, yet a slug initially persists above it. Such a continuous process subsequently leads to the initial expansion of the bed, and causes a delay of at least 30 s between the beginning of stirring and initiation of fluidization.

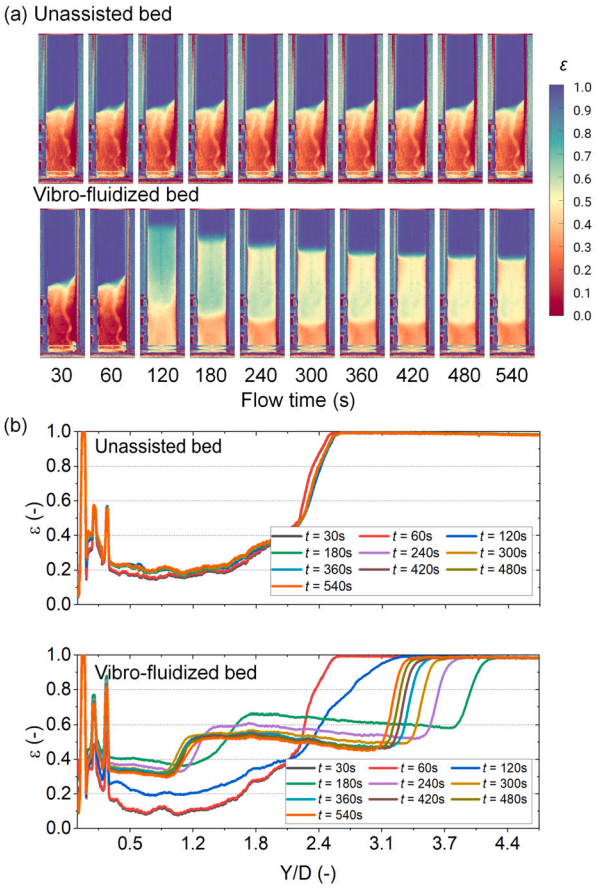

Fig. 6. (a) Time-averaged flow patterns and (b) gas fraction profile in the unassisted and vibro-fluidized beds. Each flow pattern is obtained by averaging 10 s of frames at each time. Vibration starts at 120 s after the fluidization process begins. $U = 3.1$ cm/s; $f = 30$ Hz; $A = 1.0$ mm, $D = 5$ cm, $H_0 = 10$ cm.

Increasing rotation speed results in a more pronounced development of fluidization. The flow patterns presented in Fig. 7a demonstrate that a rotation speed of 35 rpm is insufficient to achieve a homogeneous fluidization state in the bed. The gas flow tends to concentrate towards the central region, where the shaft is located, indicating that the existing powder structure remains largely intact. Fig. 7b displays an overshoot of bed expansion at 130 rpm, reaching a peak approximately 60 s after the stirring begins. The results suggest the existence of a threshold rotation speed required for initiating a fully developed fluidization state, which in this set-up was observed above 70 rpm, corresponding to a tip speed of 10.5 cm/s. However, excessively high rotation speeds lead to the rapid displacement of particles, preventing them from entering the sweeping zone. This separation results in the formation of an air pocket - a stable, particle-free region around the stirrer stack - which greatly reduces the contacts between particles and stirrers, as shown at 180 s for 160 rpm, therefore delaying the initialization of fluidization. At larger rotation speeds, such as 230 rpm, an air pocket forms and persists, and the primary bed structure remains largely untouched, since the blade rotates without impacting powder or inputting any mechanical energy. Consequently, the gas flow tends to bypass the central region around the shaft, continuously propelling particles to both sides and creating a funnel-like configuration at the top of the bed.

Additionally, the flow patterns show that, over time, particles tend to accumulate along the sidewalls of the column, resulting in reduced bed expansion. Although there are variations in the maximum expansion levels, the bed expansion at all tested rotation speeds eventually converges to a similar H/H_0 of approximately 1.5, with the exception of the bed at 160 rpm, which experienced delayed fluidization initia-

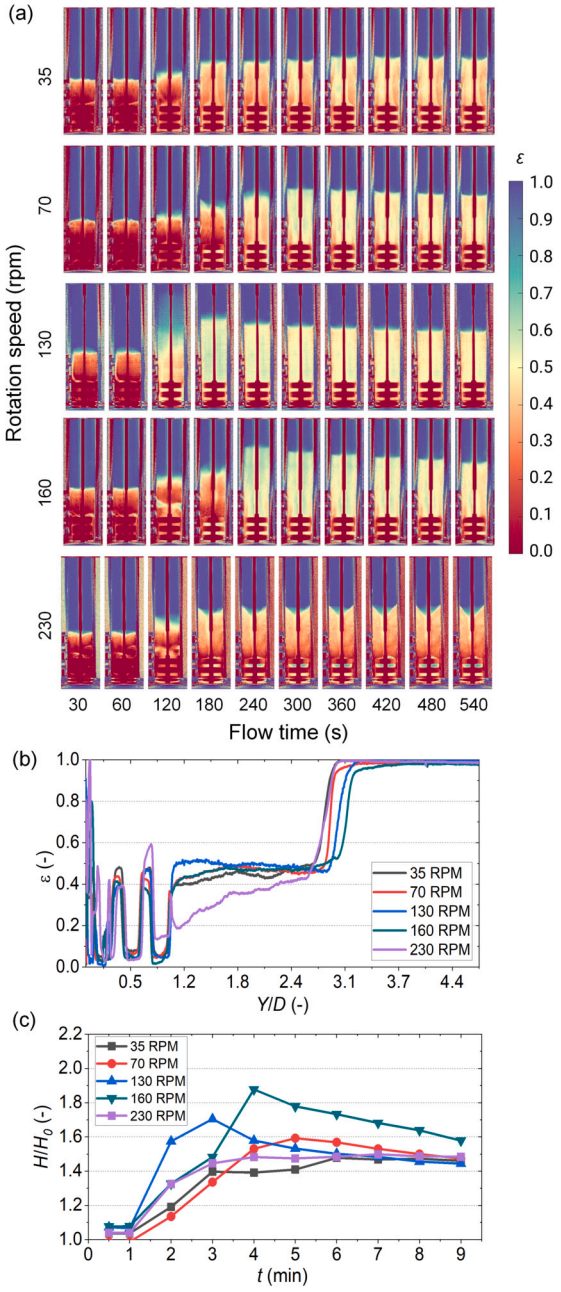

Fig. 7. (a) Time-averaged flow patterns in stirred beds of varying rotation speed from 35 rpm to 230 rpm, and (b) the gas fraction at 540 s and (c) bed expansion profiles. Stirring starts at 120 s after the fluidization process begins. The flow pattern and profiles are obtained by averaging 10 s of frames at each selected time. Three stirrers of four blades are used. $U = 3.1$ cm/s, $D = 5$ cm, $H_0 = 10$ cm.

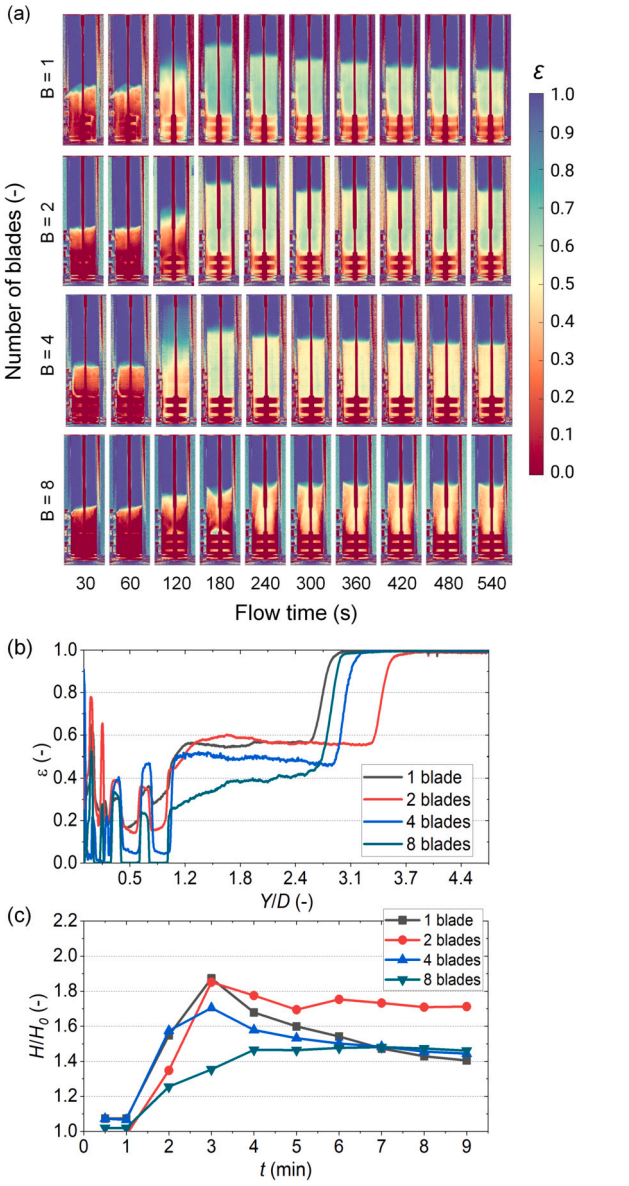

Fig. 8. (a) Time-averaged flow patterns in stirred beds of varying number of blades from one to eight, and (b) the gas fraction at 540 s. Stirring starts at 120 s after the fluidization process begins. The flow pattern and profiles are obtained by averaging 10 s of frames at each selected time. A stack of 3 stirrers is used, operating at 130 rpm. $U = 3.1$ cm/s, $D = 5$ cm, $H_0 = 10$ cm.

tion, as shown in Fig. 7c. This is consistent with the previously reported bed expansions for this powder in a vibro-fluidized bed (Kamphorst et al., 2024a). On the other hand, Fig. 7b displays that at rotation speeds of 70 rpm and above, the beds exhibit similar gas fractions around $\varepsilon = 0.5$, despite the slight differences in bed expansion, suggesting the attainment of comparable fluidization with each other.

3.3. Effect of number of blades

Increasing the number of blades makes the initialization of fluidization more challenging. As depicted in Fig. 8a, a single-bladed stirrer leads to immediate collapse of the existing powder structure, resulting in rapid bed expansion. However, such a dilated state is not sustained, and the bed quickly contracts. In contrast, stirrers equipped with eight blades initially render an air pocket (as shown at 180 s), and gradually cause the bed to spout, with a substantial number of particles being directed towards the walls, which impairs the interphase contacts. Consequently, instead of evolving into an effective fluidization state, the bed creates a pronounced preferential path for gas to bypass around the shaft in the central region.

According to Fig. 8b and Fig. 8c, configurations with double-bladed stirrers outperform others in terms of bed expansion and gas fraction. For the configurations with one and four blades, despite achieving initial fluidization, bed expansion begins to decline over time, eventually converging to a similar bed expansion, indicative of poor sustaining fluidization. Based on the flow patterns, an increased number of blades leads to more pronounced stratification in the gas-solid suspension, creating preferential gas pathways at the center and reduced particle dilation.

Table 2
Disturbance frequencies tested.

Blade number B [-]	Area blockage A_B [-]	Rotation speed, R [rpm]				
		35	70	130	160	230
1	15.97%	-	-	130	-	-
2	18.97%	-	-	260	-	-
4	24.98%	140	280	520	640	920
8	37.00%	-	-	1040	-	-

However, increasing the number of blades at a fixed rotation speed has a twofold effect: it enhances the disturbance frequency (a product of the blade number and rotation speed), but also increases obstruction in the cross-sectional area for gas distribution. Fluidization behavior cannot be solely characterized by disturbance frequency, as detailed in Table 2. For instance, the configuration with two blades at 130 rpm and the configuration with four blades at 70 rpm yield comparable disturbance frequencies, yet the latter displays much inferior fluidization. The performance is influenced by both the absolute impact speed (e.g., tip speed) and the coverage of the cross-sectional area.

3.4. Effect of number of stirrers

To determine the influence of stirrer number on fluidization, experiments were performed at a consistent rotation speed of 130 rpm, while varying the number of stirrers from one to six. Stacks of four-blade stirrers were used as the basic stirrer block. Increasing the number of stirrers occupies more space inside the powder bed, slightly elevating the static bed height, but also results in a decrease in bed expansion, as shown in Fig. 9.

With the use of more stirrers, a greater fraction of particles is swept across the bed. It is noteworthy that, with six stirrers, the sweep length approaches the static bed height. This increased effective stirring volume creates a taller compacted phase within the bed induced by the stirrer blades. Consequently, it promotes the formation of the central gas pathway. Fig. 9c shows a rapid decline in bed expansion after only 120 s of stirring. The flow pattern is similar to the one obtained with an eight-blade configuration in Fig. 8a, where the preferential pathway allows upward spouting of particles, eventually leading to a funnel-like bed surface. Conversely, fewer stirrers develop higher initial bed expansion as well as sustaining a more homogeneous fluidization. The bed expansion ratios of the one and three stirrer configurations approach approximately the same value after 540 s, whereas the double-stirrer configuration demonstrates enhanced maintenance of effective bed fluidization. Single- and double-stirrer configurations were observed to initiate fluidization rapidly, resulting in a steadily homogeneous fluidization state. Overall, an increase in the number of stirrers has a tendency to lead to degraded and more inhomogeneous fluidization.

In several experiments, such as those combining one or three stirrers with four or eight blades, a persistent air pocket formed, remaining stable throughout the experiment and hindering the initiation of fluidization. It is noteworthy that the single-blade stirrer configuration did not result in the formation of an air pocket in any scenario. In particular, the flow pattern observed with a single stirrer configuration exhibits less particle accumulation on the walls. This phenomenon is potentially attributed to its asymmetric design, which facilitates more complex gas and bubbles distribution and encourages particle recirculation. Therefore, it is likely that an asymmetrical stirrer design is advantageous for sustaining fluidization, while a suitable combination of sufficient tip speed and cross-section opening is crucial to disrupt existing structures in the bed, such as channels and air pockets, thereby initiating fluidization. Furthermore, stirring the bottom region is of critical importance, as demonstrated by the experiment shown in Fig. 10, in which a two-bladed stirrer positioned in the middle of the static bed was ineffective in initiating fluidization. Such a mid-level stirring only led to the forma-

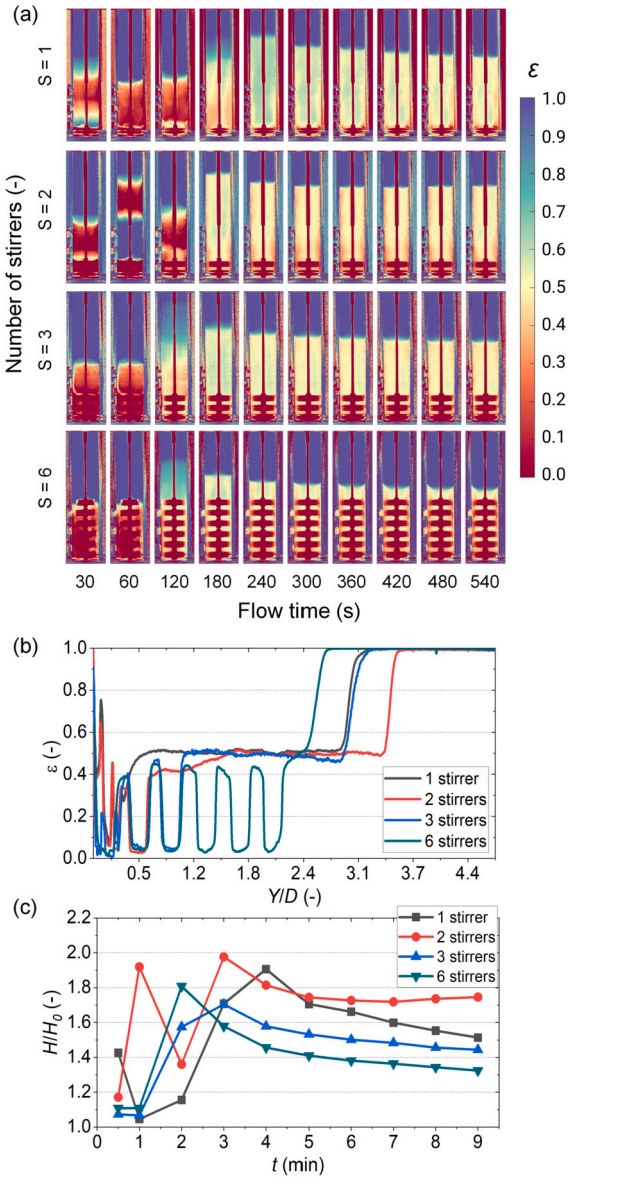

Fig. 9. Time-averaged flow patterns in stirred beds of varying number of stirrers from one to six, and (b) the gas fraction at 540 s. Stirring starts at 120 s after the fluidization process begins. The flow pattern and profiles are obtained by averaging 10 s of frames at each selected time. Four-bladed stirrers are used, operating at 130 rpm. $U = 3.1$ cm/s, $D = 5$ cm, $H_0 = 10$ cm.

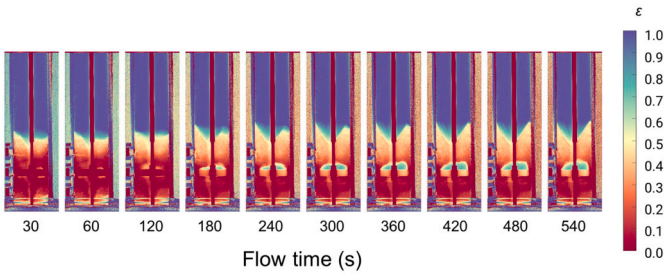

Fig. 10. Time-averaged flow patterns in the stirred bed. The stirrer is positioned in the middle of the static bed ($Y = 5$ cm). Stirring starts at 120 s after the fluidization process begins. The flow pattern and profiles are obtained by averaging 10 s of frames at each selected time. A two-bladed stirrer is used, operating at 130 rpm. $U = 3.1$ cm/s, $D = 5$ cm, $H_0 = 10$ cm.

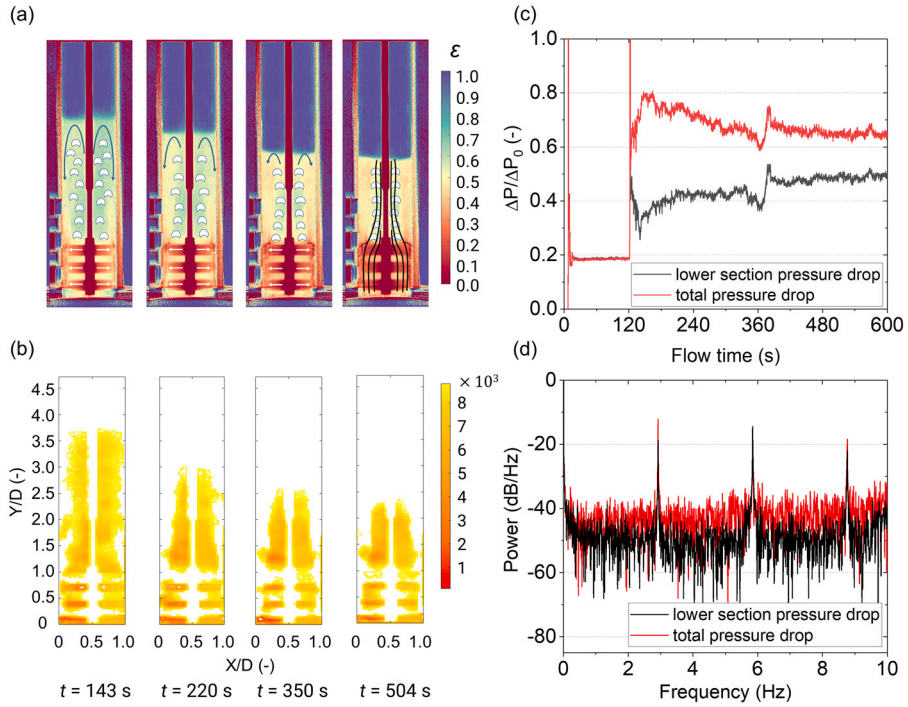

Fig. 11. Example flow behavior in a stirred bed with three double-bladed stirrers at 175 rpm: (a) Time-averaged flow patterns with indicative bubbles, and arrows suggesting the solid circulation routes, and streamlines showing the gas and bubbles routes; (b) the corresponding bubble probability density map; (c) the corresponding pressure series, measured over the entire bed and the bottom to $2/3^{rd}$ of initial bed height and (d) power spectrum. The flow pattern and profiles are obtained by averaging 10 s of frames at each selected time. $U = 3.1$ cm/s, $D = 5$ cm, $H_0 = 10$ cm.

tion of an air pocket in the stirred area, aligning with the conclusions in Godard and Richardson (1969).

Additionally, brief episodes of vertical vibration (with an amplitude of 1 mm and a frequency of 30 Hz) have shown effective in initiating fluidization, preventing the formation of air pockets regardless of the stirrer configurations; however, it was discovered that vibration induces significant powder stratification within the bed, which depresses the maintenance of the fluidized state. Therefore, such a combination of stirring and vibration is not considered favorable (See section 3 of the Supplementary Material for the experimental results).

3.5. Advanced design of stirrer

The flow patterns observed show that most modular designs, following the shape shown in Fig. 4, are not capable of maintaining a highly expanded state. Overall, the modular stirrers exhibit a tendency to press the particles against the walls, inducing poor interphase contact. For demonstration purpose, Fig. 11a and Fig. 11b illustrate various stages of flow patterns and the bubbling probability density of a stirred bed operating at 175 rpm with three stirrers of two blades, where this issue is particularly pronounced. The observed flow patterns show that, following the initial bed expansion, particles begin to accumulate along the walls and directly above the distributor plate in regions not reached by the stirrers. Subsequently, the particles form a stable structure that restricts gas flow, causing bubbles and gas to divert towards the bed central regions, as shown in Fig. 11a with added illustrated bubbles and streamlines for clearer understanding of the gas pathways. Meanwhile, bubble-free regions in close proximity to the sidewall continue to develop. Eventually, the particle structure becomes stable, without recirculation of solids in the side and bottom regions of the bed, forming an annular ring of the stagnant particle phase. In contrast, the gas flow and bubbles consistently travel the central region and spout particles upwards, creating a funnel-like surface at the top of the bed. Overall, the bed deteriorates into a radially stratified system characterized by insufficient interphase contacts.

In Fig. 11c and Fig. 11d, the time series of normalized pressure drops and their power spectra are displayed, respectively. The pressure drop of both the bottom section and the total bed sharply increases upon the initiation of the mechanical agitation at 120 s. In the subsequent 20 s, a decrease in the pressure drop in the bottom bed is noted, whereas the total pressure drop increases, indicating dilution of the bed and internal mixing. However, for the remaining duration of the experiment, the opposite was observed: the total pressure drop decreases, whereas it increases in the bottom section, suggesting a densification of the bed, specifically in the bottom section, as shown in Fig. 11a. Additionally, the power spectra of the pressure drop signals exhibit distinct peaks at the frequency of full stirrer rotation ($f = 2.92$ Hz), and the disturbance frequency linked with individual blades passing by the probe ($f = 5.84$ Hz).

The witnessed fluidization behavior provides insight into several design criteria for improving stirrer configurations. Firstly, the stirrer design should aim to maximize the sweep area to ensure consistent mobility of the powder, particularly in the bottom and wall regions of the bed. To corroborate this hypothesis, a modification to the stirrer is proposed, designed to reactivate particles that have settled in these critical regions. Lowering the stirrers is not feasible, since the tip of the bottom shaft was already positioned close to the distributor plate, only 5 mm away. As an alternative, attaching a soft brush to the lowest stirrer enables gently contacts with the plate and column walls, sweeping the deposited particles. Such a modification would facilitate in reciculating the powder into the fluidization process. A modular design consisting of three stirrers, each with four blades, served as the reference geometry, and experiments were conducted at a rotation speed of 130 rpm. From this reference configuration, two variations of soft brush arrangements were tested. The first design positions the soft brushes solely on the bottom surface of the lowest stirrer, and the second layout features soft brushes affixed to both the side and bottom of the lowest stirrer, allowing for the simultaneous sweeping of the wall and bottom areas above the distributor plate, as shown in Fig. 12.

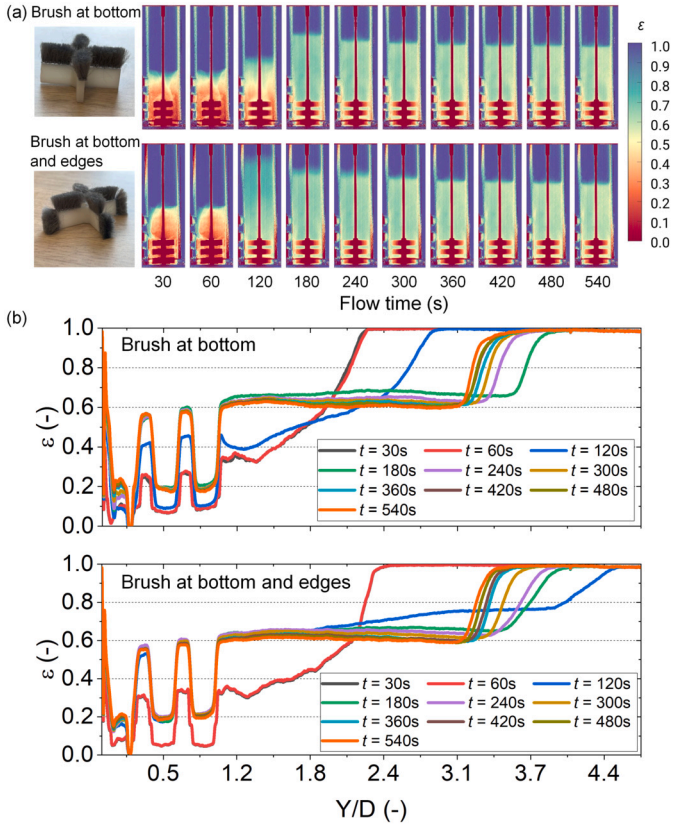

Fig. 12. (a) Time-averaged flow patterns and (b) gas fraction profile in the stirred beds with brushes attached. Stirring starts at 120 s after the fluidization process begins. Each flow pattern is obtained by averaging 10 s of frames at each time. $U = 3.1$ cm/s, $N = 130$ rpm, $D = 5$ cm, $H_0 = 10$ cm.

An improvement in fluidization is discernible with the integration of soft brushes, as depicted in Fig. 12b. Both brush designs result in a similar initial bed expansion, and fluidization degradation is considerably reduced with the brush implementation. The bed stabilized after 300 s, and maintained a consistent, homogeneous state of fluidization. Compared to the experiments shown in Fig. 7, the flow patterns displayed a much more uniform fluidization across the entire bed. Furthermore, the flow patterns revealed particle accumulation along the sidewalls, where brushes are absent, but notably, particles at the bed bottom are effectively recirculated in both scenarios, promoting sustainable solid circulation. While the difference between the two brush designs is marginal, there is an improvement in terms of particle aeration, as indicated by the increased gas fraction. In contrast, experiments with non-brush modular stirrers showed a continuous compaction of solids. The successful implementation of brushes, as proof of concept, highlights the importance of thoroughly sweeping the bottom region to ensure effective circulation of particles. It is worth noting that in large-scale applications, the volume beneath the stirrers may only constitute a relatively small portion of the total powder load. Nonetheless, this region plays a crucial role in shaping the gas distribution, making it imperative to avoid any structured accumulation of particles.

In addition, the stirrer design should promote a more even distribution of bubbles and gas throughout the bed, while also preserving as much of the cross-sectional area as possible. This approach enables high shear interactions between gas and solids and minimizes the likelihood of air pocket formation. In addition to the modular design analysis, various modifications and several advanced stirrer configurations were also explored, as a proof of concept. These are depicted in Fig. 13. The designs aim to fulfill the identified design criteria for enhanced fluidization performance by introducing both radial and axial disturbances. Specifically, three intricate configurations: the helical ribbon,

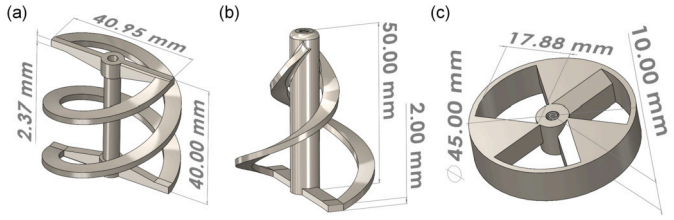

Fig. 13. Configurations of advanced stirrers (a) ribbon type stirrer (b) spiral type stirrer (c) rotary disc.

spiral ribbon, and double spiral ribbon stirrer, were tested. These stirrers maintain a height comparable to the stacked three-stirrer modular configurations, but feature a curved spine and ribbon geometry. This design is anticipated to lift particles, instead of pressing them to the sides. The spiral ribbon mixers modify the gas pathway with cone-shaped rings positioned centrally, effectively redirecting gas streams and bubbles to create a more dynamic gas distribution. For consistency, all comparisons were also conducted at a rotation speed of 130 rpm, allowing for a direct comparison of their effectiveness in fluidization against the standard modular configurations.

The experimental results shown in Fig. 14 reveal that the ribbon stirrer falls short in promoting bed expansion or disrupting the existing bed structure. Despite the stirring, gas continues to bypass through the central region, similar to the flow pattern obtained with the three-stirrer eight-blade configuration in Fig. 8, which is attributed to its relatively hollow and symmetrical configuration, coupled with gas blockage near the edges. In contrast, the use of a single spiral stirrer is able to trigger an initial bed expansion, while the particles quickly begin to accumulate, clearly visible along the cone edges. The results indicate that the single spiral stirrer converges gas streams at the tip of its cone, leading to a stable state with a slightly higher gas fraction of 0.5, compared to the ribbon stirrers, in which the gas fraction remains at 0.4. In an effort to redistribute gas flow, a configuration featuring two opposing spiral stirrers mounted in an inverted arrangement was tested. This configuration is anticipated to redistribute the merged gas flow from the tip of the lower spiral stirrer. The flow patterns reveal that such a configuration rapidly initiated bed expansion, and the top region was fluidized with a more uniform distribution of gas and bubbles, thereby maintaining a high level of bed expansion. Despite some particles settling from the gap between the stirrer edge and column wall, the enhanced distribution results in less particle accumulation along the sidewalls. The fluidization achieved with this configuration remains stable over time, exhibiting a significant dilated bed with a gas fraction ε exceeding 0.7.

Lastly, the influence of cross-sectional area openings on fluidization was investigated using different arrangements of rotary discs. The designs feature three triangular-shaped openings, as shown in Fig. 13c. Both aligned and alternating arrangements were assessed, accounting for 50% and 100% of cross-sectional area obstruction, respectively. In the case of the 100% obstruction arrangement, the gas is unable to pass axially through the column, but navigates tortuously through the gaps between adjacent stirrers.

Fig. 15 illustrates the effect of stirrer-induced cross-sectional area blockage on fluidization behavior. Fluidization becomes increasingly challenging, as the level of obstruction increases. Beds stirred by rotary discs in both the aligned and alternating arrangements are incapable of achieving a homogeneous state of fluidization. The aligned configuration is able to trigger initial bed expansion, but instead of improving fluidization by redistributing gas flow, fluidization rapidly deteriorates as particles accumulate along the sides, resulting in a spouting state. The half-opening configuration, designed to continuously redirect gas streams through the available openings, also shows it is ineffective in assisting fluidization. In contrast, the alternating arrangement faces greater challenges in initiating fluidization. Air pockets remain prevalent throughout the fluidization process, leading to a significant spouted bed state, as shown in Fig. 15b. This comparison suggests that the tor-

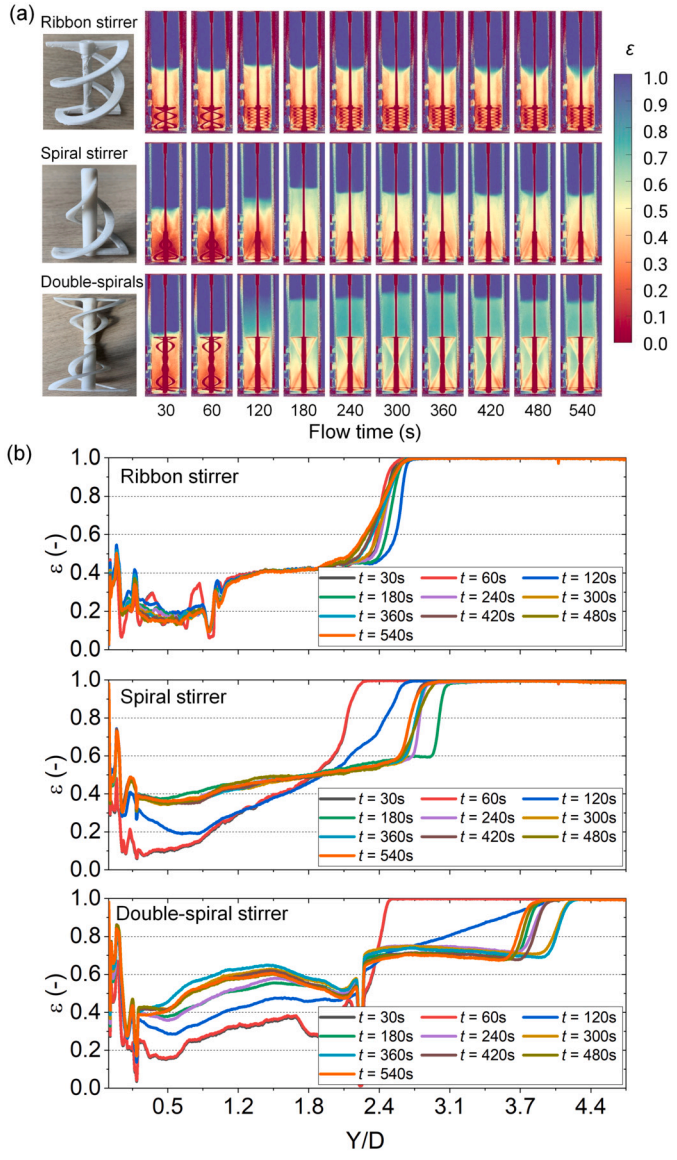

Fig. 14. (a) Time-averaged flow patterns and (b) gas fraction profile in the unassisted and vibro-fluidized beds. Each flow pattern is obtained by averaging 10 s of frames at each time. Stirring starts at 120 s after the fluidization process begins. $U = 3.1$ cm/s, $N = 130$ rpm, $D = 5$ cm, $H_0 = 10$ cm.

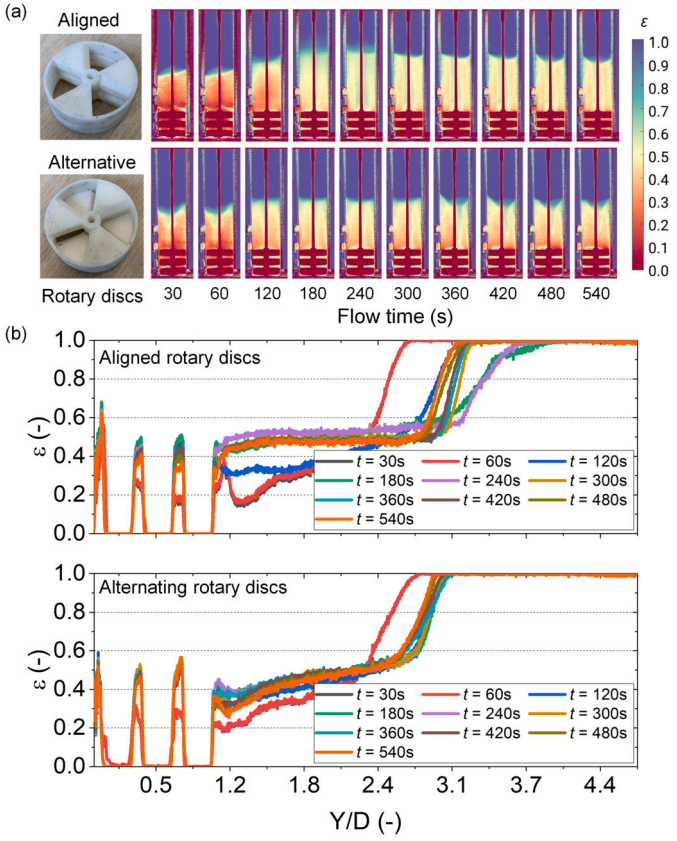

Fig. 15. (a) Time-averaged flow patterns and (b) gas fraction profile in the bed with different cross-section blockage. Each flow pattern is obtained by averaging 10 s of frames at each time. Stirring starts at 120 s after the fluidization process begins. $U = 3.1$ cm/s, $N = 130$ rpm, $D = 5$ cm, $H_0 = 10$ cm.

tuous gas pathways created in this setup are detrimental to initiating fluidization. These findings align with the observations of increased blockage when the number of blades is increased, as previously shown in Fig. 8.

The conducted experiments showcase that the proposed design criteria for stirrers are promising. Notable improvements were observed in both bed expansion and sustained aeration in comparison to modular designs. However, practical applications present additional concerns. Scaling up stirrers is not trivial and can be approached either through employing multiple stirrers in specific areas or a single, larger-sized stirrer. Therefore, replicating these experiments in a larger column would yield valuable insights.

In addition to stirrer configurations, the observed flow patterns reveal that the presence of the shaft throughout the bed is problematic. Its substantial size (10% of the bed diameter) is promoting a preferential pathway for gas-bypass. It might be preferable to introduce the shaft from the bottom of the bed, thereby avoiding the formation of a central gas pathway. Nevertheless, such a negative effect is anticipated to diminish if a larger bed diameter is employed, which would proportionally reduce the relative size of the shaft.

Moreover, achieving a balance between the blade length and volume swept by the blades is crucial. An excessively long blade could continuously press particles towards the bed boundaries, leading to inefficient mixing and potential compaction. In contrast, a blade that is too short may be inadequate for effectively sweeping the powder bed and initiating fluidization.

4. Conclusions

Stirring assistance has been shown to be an effective method for initiating fluidization by collapsing the existing bed structure, expanding the bed, and converting a channeling bed into a bubbling one by reactivating settled particles. The fluidization of cohesive micron-silica powders is heavily influenced by the stirring conditions and the configuration of the stirrer. Designs with comb-configuration featuring fewer stirrers and blades, particularly when positioned in the bottom region of the bed, are more effective than those with a larger number of stirrers and blades in both initiating and sustaining fluidization. It has been observed that an increased number of stirrers tends to sweep more particles towards the column walls, resulting in a compacted layer of stagnant solids. This layer restricts the effective cross-sectional area, and redirects gas and bubbles towards a central pathway alongside the shaft. Besides, stirring agitation should be sufficiently vigorous to disrupt the internal structure of the bed, while excessive stirring can prevent particles from entering the stirring zone and quickly push them towards the sides, causing poor contact between the stirrer and the particles.

The analysis of flow patterns highlights that the compacted phase of solids is detrimental to effective fluidization. It is essential to either prevent the formation of stagnant zones or reactivate settled solids to sustain a fluidized state. Consequently, it is advisable to maximize sweep coverage to reduce stagnant areas and prevent compaction and deposition of solids. In addition, implementing more intricate designs, especially those that are asymmetrical, can facilitate the redistribution of gas and bubbles, and thereby promoting solid circulation. The configurations should also preserve an adequate opening in the cross-sectional area and avoid creating tortuous gas pathways. To formulate a more quantitative assessment, future research can focus on measuring the torque exerted by the stirrer on the system. This measure could serve as an additional indicator for optimizing stirrer configurations, potentially correlating it with the minimum mechanical energy input necessary to initiate and sustain an effective fluidization state. Moreover, to further understand radial and axial mixing within this system, particle tracking techniques could be employed.

CRediT authorship contribution statement

Kaiqiao Wu: Writing – original draft, Visualization, Validation, Software, Methodology, Investigation, Formal analysis, Data curation, Conceptualization. **Rens Kamphorst:** Writing – review & editing, Visualization, Validation, Investigation, Formal analysis, Data curation. **Anna Bakker:** Writing – review & editing, Software, Investigation, Formal analysis, Data curation. **Jasper Ford:** Software, Investigation, Data curation. **Evert C. Wagner:** Writing – review & editing, Resources, Methodology. **Olga Ochkin-Koenig:** Writing – review & editing, Methodology, Investigation. **Miika Franck:** Writing – review & editing, Methodology, Investigation. **Dominik Weis:** Writing – review & editing, Software, Methodology, Investigation. **Gabrie M.H. Meesters:** Writing – review & editing, Supervision, Project administration, Methodology, Funding acquisition, Conceptualization. **J. Ruud van Ommen:** Writing – review & editing, Supervision, Project administration, Methodology, Funding acquisition, Conceptualization.

Declaration of competing interest

The authors declare that they have no known competing financial interests or personal relationships that could have appeared to influence the work reported in this paper.

Data availability

Data will be made available on request.

Acknowledgements

The research leading to these results has received funding from BASF SE and the Dutch Research Council (NWO) (ENPPS.LIFT.019.027). Additionally, this work is part of the Advanced Research Center for Chemical Building Blocks, ARC CBBC, which is co-founded and co-financed by the Dutch Research Council (NWO) and the Netherlands Ministry of Economic Affairs and Climate Policy (2020.023.A.TUD.1).

Appendix A. Supplementary material

Supplementary material related to this article can be found online at https://doi.org/10.1016/j.ces.2024.120069.

References

Alavi, S., Caussat, B., 2005. Experimental study on fluidization of micronic powders. Powder Technol. 157 (1), 114–120. https://doi.org/10.1016/j.powtec.2005.05.017.

Beakawi Al-Hashemi, H.M., Baghabra Al-Amoudi, O.S., 2018. A review on the angle of repose of granular materials. Powder Technol. 330, 397–417. https://doi.org/10.1016/j.powtec.2018.02.003.

Boyce, C.M., Rice, N.P., Ozel, A., Davidson, J.F., Sederman, A.J., Gladden, L.F., Sundaresan, S., Dennis, J.S., Holland, D.J., 2016. Magnetic resonance characterization of coupled gas and particle dynamics in a bubbling fluidized bed. Phys. Rev. Fluids 1 (7), 074201. https://doi.org/10.1103/PhysRevFluids.1.074201.

Bradley, D., Roth, G., 2007. Adaptive thresholding using the integral image. J. Graph. Tools 12 (2), 13–21. https://doi.org/10.1080/2151237X.2007.10129236.

Chandrasekera, T., Wang, A., Holland, D., Marashdeh, Q., Pore, M., Wang, F., Sederman, A., Fan, L., Gladden, L., Dennis, J., 2012. A comparison of magnetic resonance imaging and electrical capacitance tomography: an air jet through a bed of particles. Powder Technol. 227, 86–95. https://doi.org/10.1016/j.powtec.2012.03.005.

Cruz, M.A.A., Passos, M.L., Ferreira, W.R., 2005. Final drying of whole milk powder in vibrated-fluidized beds. Dry. Technol. 23 (9–11), 2021–2037. https://doi.org/10.1080/07373930500210473.

Francía, V., Wu, K., Coppens, M.-O., 2021. Dynamically structured fluidization: oscillating the gas flow and other opportunities to intensify gas-solid fluidized bed operation. Chem. Eng. Process. Process Intensific. 159, 108143. https://doi.org/10.1016/j.cep.2020.108143.

Gidaspow, D., Bezburuah, R., Ding, J., 1991. Hydrodynamics of circulating fluidized beds: kinetic theory approach. In: Proc. of 7th Eng. Found. Conf. on Fluidization, pp. 75–82. https://www.osti.gov/biblio/5896246.

Godard, K., Richardson, J., 1969. The use of slow speed stirring to initiate particulate fluidisation. Chem. Eng. Sci. 24 (1), 194–195. https://doi.org/10.1016/0009-2509(69)80022-9.

Helmi, A., Wagner, E.C., Gallucci, F., van Sint Annaland, M., van Ommen, J.R., Mudde, R.F., 2017. On the hydrodynamics of membrane assisted fluidized bed reactors using x-ray analysis. Chem. Eng. Process. Process Intensific. 122, 508–522. https://doi.org/10.1016/j.cep.2017.05.006.

Hong, R., Ding, J., Li, H., 2005. Fluidization of fine powders in fluidized beds with an upward or a downward air jet. Particuology 3 (3), 181–186. https://doi.org/10.1016/S1672-2515(07)60083-9.

Hu, C., Zhang, P., Wang, X., Yang, X., Yang, L., Zhang, Z., Kong, X., 2020. Improvement of fluidization quality of a lif bed using internal blades. Powder Technol. 362, 817–825. https://doi.org/10.1016/j.powtec.2019.12.008.

Kamphorst, R., Wu, K., Salameh, S., Meesters, G.M.H., van Ommen, J.R., 2023. On the fluidization of cohesive powders: differences and similarities between micro- and nano-sized particle gas–solid fluidization. Can. J. Chem. Eng. 101 (1), 227–243. https://doi.org/10.1002/cjce.24615.

Kamphorst, R., van der Sande, P.C., Wu, K., Wagner, E.C., David, M., Meester, G.M.H., van Ommen, J.R., 2024a. The mechanism behind vibration assisted fluidization of cohesive micro-silica. KONA Powder Part. J. 41, 254–264. https://doi.org/10.14356/kona.2024007.

Kamphorst, R., Wu, K., van Baarlen, M., Meesters, G.M., van Ommen, J.R., 2024b. Effect of vibrational modes on fluidization characteristics and solid distribution of cohesive micro- and nano-silica powders. Chem. Eng. Sci. 291, 119911. https://doi.org/10.1016/j.ces.2024.119911.

Kariman, A., Rao, V., Farjpourlar, M., 2013. Fluidization characteristics of nano particles with the assist of stirrer. IOSR J. Appl. Phys. 5, 24–27. https://doi.org/10.9790/4861-0532427.

Khosravi Bizhaem, H., Basirat Tabrizi, H., 2013. Experimental study on hydrodynamic characteristics of gas-olid pulsed fluidized bed. Powder Technol. 237, 14–23. https://doi.org/10.1016/j.powtec.2013.01.001.

Kim, J., Han, G.Y., 2006. Effect of agitation on fluidization characteristics of fine particles in a fluidized bed. Powder Technol. 166 (3), 113–122. https://doi.org/10.1016/j.powtec.2006.06.001.

King, D.M., Liang, X., Zhou, Y., Carney, C.S., Hakim, L.F., Li, P., Weimer, A.W., 2008. Atomic layer deposition of tio2 films on particles in a fluidized bed reactor. Powder Technol. 183 (3), 356–363. https://doi.org/10.1016/j.powtec.2008.01.025.

Kuipers, N., Stamhuis, E., Beenackers, A., 1996. Fluidization of potato starch in a stirred vibrating fluidized bed. Chem. Eng. Sci. 51 (11), 2727–2732. https://doi.org/10.1016/0009-2509(96)00143-1.

Ma, J., van Ommen, J.R., Liu, D., Mudde, R.F., Chen, X., Wagner, E.C., Liang, C., 2019. Fluidization dynamics of cohesive geldart B particles. Part I: X-ray tomography analysis. Chem. Eng. J. 359, 1024–1034. https://doi.org/10.1016/j.cej.2018.11.082.

Makkawi, Y., Wright, P., 2002. Fluidization regimes in a conventional fluidized bed characterized by means of electrical capacitance tomography. Chem. Eng. Sci. 57 (13), 2411–2437. https://doi.org/10.1016/S0009-2509(02)00138-0.

Maurer, S., Wagner, E.C., van Ommen, J.R., Schildhauer, T.J., Teske, S.L., Biollaz, S.M.A., Wokaun, A., Mudde, R.F., 2015. Influence of vertical internals on a bubbling fluidized bed characterized by X-ray tomography. Int. J. Multiph. Flow 75, 237–249. https://doi.org/10.1016/j.ijmultiphaseflow.2015.06.001.

Mema, I., Wagner, E.C., van Ommen, J.R., Padding, J.T., 2020. Fluidization of spherical versus elongated particles - experimental investigation using X-ray tomography. Chem. Eng. J. 397, 125203. https://doi.org/10.1016/j.cej.2020.125203.

Mudde, R.F., 2010. Time-resolved x-ray tomography of a fluidized bed. Powder Technol. 199 (1), 55–59. https://doi.org/10.1016/j.powtec.2009.04.021.

Penn, A., Boyce, C.M., Conzelmann, N., Bezinge, G., Pruessmann, K.P., Müller, C.R., 2019. Real-time magnetic resonance imaging of fluidized beds with internals. Chem. Eng. Sci. 198, 117–123. https://doi.org/10.1016/j.ces.2018.12.041.

Quevedo, J.A., Omosebi, A., Pfeffer, R., 2010. Fluidization enhancement of agglomerates of metal oxide nanopowders by microjets. AIChE J. 56 (6), 1456–1468. https://doi.org/10.1002/aic.12075.

Raganati, F., Chirone, R., Ammendola, P., 2018. Gas-solid fluidization of cohesive powders. Chem. Eng. Res. Des. 133, 347–387. https://doi.org/10.1016/j.cherd.2018.03.034.

Saayman, J., Nicol, W., van Ommen, J.R., Mudde, R.F., 2013. Fast x-ray tomography for the quantification of the bubbling-, turbulent- and fast fluidization-flow regimes and void structures. Chem. Eng. J. 234, 437–447. https://doi.org/10.1016/j.cej.2013.09.008.

van Ommen, J.R., Mudde, R.F. Measuring the gas-solids distribution in fluidized beds – a review. Int. J. Chem. React. Eng. 6 (1). https://doi.org/10.2202/1542-6580.1796.

van Ommen, J.R., Nijenhuis, J., Coppens, M.-O., 2009. Reshaping the structure of fluidized beds. Chem. Eng. Prog., 49–57.

van Ommen, J.R., Sasic, S., van der Schaaf, J., Gheorghiu, S., Johnsson, F., Coppens, M.-O., 2011. Time-series analysis of pressure fluctuations in gas-solid fluidized beds - a review. Int. J. Multiph. Flow 37 (5), 403–428. https://doi.org/10.1016/j.ijmultiphaseflow.2010.12.007.

van Ommen, J.R., Valverde, J.M., Pfeffer, R., 2012. Fluidization of nanopowders: a review. J. Nanopart. Res. 14 (3), 737. https://doi.org/10.1007/s11051-012-0737-4.

van Ommen, J.R., King, D.M., Weimer, A., Pfeffer, R., van Wachem, B., Johnson, S., Looije, N., 2013. Experiments and modelling of micro-jet assisted fluidization of nanopowder. In: Knowlton, P.E.T. (Ed.), 10th International Conference on Circulating Fluidized Beds and Fluidization Technology (CFB-10). In: ECI Symposium Series. https://dc.engconfintl.org/cfb10/43.

Wu, K., de Martín, L., Coppens, M.-O., 2017. Pattern formation in pulsed gas-solid fluidized beds: the role of granular solid mechanics. Chem. Eng. J. 329, 4–14. https://doi.org/10.1016/j.cej.2017.05.152.

Wu, K., Galli, F., de Tommaso, J., Patience, G.S., van Ommen, J.R., 2023a. Experimental methods in chemical engineering: pressure. Can. J. Chem. Eng. 101 (1), 41–58. https://doi.org/10.1002/cjce.24533.

Wu, K., Wagner, E.C., Ochkin-Koenig, O., Franck, M., Weis, D., Meesters, G.M.H., Ruud van Ommen, J., 2023b. Time-resolved x-ray study of assisted fluidization of cohesive micron powder: on the role of mechanical vibration. Chem. Eng. J., 143936. https://doi.org/10.1016/j.cej.2023.143936.

Yang, F., Wang, L., Yin, S., Li, Y., Liu, C., Tong, L., 2013. Experimental study on the entrainment characteristics of ultrafine powder in a fluidized bed with vibrator and agitator. Ind. Eng. Chem. Res. 52 (3), 1359–1364. https://doi.org/10.1021/ie301733t.

Yin, S.-W., Wang, L., Liu, C.-P., 2008. Study on agglomerate breaking and feeding of superfine particles in fluidized bed. Chin. J. Process Eng. 8 (2), 230. www.jproeng.com/EN/Y2008/V8/I2/230.

Zhang, W., 2009. A review of techniques for the process intensification of fluidized bed reactors. Chin. J. Chem. Eng. 17 (4), 688–702. https://doi.org/10.1016/S1004-9541(08)60264-5.

Zhao, Z., Liu, D., Ma, J., Chen, X., 2020. Fluidization of nanoparticle agglomerates assisted by combining vibration and stirring methods. Chem. Eng. J. 388, 124213. https://doi.org/10.1016/j.cej.2020.124213.

Zhou, Y., Zhu, J., 2019. Group C+ particles: enhanced flow and fluidization of fine powders with nano-modulation. Chem. Eng. Sci. 207, 653–662. https://doi.org/10.1016/j.ces.2019.06.056.